Co-Delivery of Multiple Small Probes to the Martian Surface

Samuel W. Albert* and Hanspeter Schaub†
University of Colorado Boulder, Boulder, CO, 80303

Regional networks comprised of small landers that fly passively through the atmosphere to a hard impact on the Martian surface represent a mission class of significant interest. As an example mission of this kind, a seismic network of six probes delivered to Cerberus Fossae is defined and relevant assumptions made, such as that the geometry and scale of the network outweigh precision landing. A linear relationship is demonstrated between jettison speed or timing and landing coordinates of the probe, and the limitations of this linear regime are quantified. A linearized targeting method is developed and employed to design a sequence of jettison events to target the desired network. Under the assumption that separation events occur mechanically via a common system, all jettison speeds are constrained to be equal. A Monte Carlo analysis is performed to quantify the impact of relevant uncertainties on the probe landing locations and resulting network geometries. These results demonstrate that, despite dispersions on jettison speeds and the resulting large variations for any given probe, the properties of the network itself remain well within the mission requirements.

I. Introduction

REGIONAL networks of small rough landers on the Martian surface are a mission class of interest to the planetary science community [1]. These missions can uniquely enable a variety of scientific investigations by taking simultaneous observations at different locations on the surface. Atmospheric science and seismology are of particular interest, and meteorological suites and microseismometers that require less than 5 kg of total payload have been developed for Mars [2, 3]. A number of network missions have been proposed or developed for Mars [4–10], but none have yet been completed successfully.

Network missions emphasize coordination over the capability or mobility of a single system, and thus benefit from minimizing the mass and volume of each probe in order to maximum their number while keeping total launch mass down. One path to lowering mass is reducing requirements such as landing accuracy and g-load that drive design of the entry, descent, and landing (EDL) system [11]. A multiprobe network mission may accommodate relaxed landing accuracy requirements because approximate distribution on the surface and accurate positioning post-landing are likely more important than precise delivery to pre-determined sites. The probes could be delivered by a single carrier spacecraft to follow uncontrolled entry trajectories, eliminating the need for attitude control or propulsion subsystems on the probes. If the carrier spacecraft then entered orbit it could serve as a telecommunications relay to Earth, provide positioning data on the landing locations, and potentially obtain complementary science measurements. Design of science instruments tolerant to relatively high landing decelerations would further reduce constraints on the EDL system.

A mission design tradeoff exists between the design of probe jettison and navigation error. If probe jettison occurs too late, the required separation velocity becomes relatively large in order to achieve the desired distribution on the surface, and there may be insufficient time to measure and correct any error introduced to the orbiter trajectory. An early separation would reduce the required jettison velocity and leave time for potential reorientation and navigation updates for the orbiter, but the relatively long coast phase amplifies the effect of any off-nominal separation velocity on the probes' trajectories and requires longer battery life prior to landing.

To gain insight into these tradeoffs, this paper defines an example Mars multiprobe mission and investigates how probes could be delivered to form regional networks of various geometries and scales on the surface. Trajectories are simulated for jettisons in the along-track and cross-track directions with varying timing and separation speed, and properties of the resulting networks are quantified. Based on these results a linearized targeting scheme is developed and demonstrated, with a discussion of the limitations of this linearization. A nominal network of 6 probes is designed to conduct regional seismology, and jettison events are designed using the linearized targeting method. Finally, the

*PhD Student, Ann and H.J. Smead Aerospace Engineering Sciences, 3775 Discovery Drive, 429 UCB – CCAR, Boulder, CO 80303. AIAA Student Member.

†Glenn L. Murphy Chair in Engineering, Ann and H.J. Smead Aerospace Engineering Sciences, 3775 Discovery Drive, 429 UCB – CCAR, Boulder, CO 80303. AIAA and AAS Fellow.

effects of relevant uncertainties on the landing locations and resulting network geometries are quantified through a 5000-trial Monte Carlo analysis.

II. Reference Mission Definition and Assumptions

As a motivating example, the reference science mission is a seismology network deployed to Cerberus Fossae, a region of known seismicity on Mars [12, 13]. A regional network in such an area can obtain useful geophysical measurements using significantly lower sensitivity seismometers than a global network would require by relying on its proximity to seismic events, bringing the required payload mass down to the range of 2–3 kg per lander* [14]. Shock-tolerant seismology payloads have been developed that can survive 15,000 g's at impact [15], and precise positioning of landers is significantly less important than achieving a network geometry that permits observability.

For the purpose of this study, the following assumptions constrain the problem:

1) Each probe is a passive ballistic rough lander
2) At least 4 probes are delivered to the surface.
3) Any two nominal landing sites are between 10 and 200 kilometers apart, and the sites are separated along 2 directions (i.e. not placed along a line).
4) Precision landing is not required.
5) The probes approach Mars on a single carrier spacecraft.
6) The probes separate from the carrier mechanically and in balanced pairs.
7) Probe jettisons occur between 5 and 0.25 days before atmospheric entry.
8) Telecom relay support is provided, either by the carrier spacecraft capturing into orbit or by existing orbital assets.

The parameters of the probes are based on the Small High Impact Energy Landing Device (SHIELD) concept, a notional entry vehicle with ballistic coefficient of approximately $\beta = 10\,\mathrm{kg\,m^{-2}}$ [16], where $\beta = m/(C_D A)$, m is vehicle mass, C_D is drag coefficient, and A is reference area. The vehicle has a lift-to-drag ratio of $L/D = 0$, and could be spin-stabilized during entry to null-out any unintended lift vector. This small probe is a rough lander designed to reduce the cost and complexity of delivering 6 kg payloads to the Martian surface by forgoing parachutes and any terminal descent system in favor of a low ballistic coefficient and crushable material, resulting in landing decelerations on the order of 1,000 Earth g's [16]. Notably, the deceleration expected at impact for the Mars Microprobes was an order of magnitude greater than this at 30,000 g's [17]. Jettisoning the probes in pairs with relative separation velocities aligned across the center of mass of the carrier spacecraft minimizes the undesired ΔV imparted to the carrier, and is a convenient way to deploy a symmetrical network geometry.

Each separation event imparts an impulsive change in velocity to the probe, where the jettison velocity $\boldsymbol{V}_j$ is defined as the velocity of the probe relative to the carrier the moment after separation, and jettison speed as the magnitude $V_j = |\boldsymbol{V}_j|$. Note that this is equivalent to impulsive $\Delta\boldsymbol{V}$, but $\boldsymbol{V}_j$ notation is used in this paper to avoid confusion with a propulsive maneuver. Because the separation events are performed mechanically (e.g., a spring jettison), it is assumed to be more desirable to match the jettison speeds between all maneuvers then it is to fully minimize their magnitudes, as long as the required separation speed is reasonably low. The carrier spacecraft is assumed to be on an entry trajectory, significantly reducing the required jettison speed for separation events.

Orbital telecom relay is assumed as a requirement for these small probes, which are unlikely to have direct-to-Earth link capability. It would be beneficial if the carrier spacecraft could enter Mars orbit and serve this purpose, especially because it would already be in the correct orbital plane to do so. For a propulsive orbit insertion, the carrier would need to perform a divert maneuver after the final probe separation to move the periapsis safely out of the atmosphere. This presents a tradeoff, because if the final probe separation occurs late then this maneuver for the carrier spacecraft becomes large and the timeline for navigation updates is short; however, if the final probe separation occurs early, the probes experience a long passive coast phase and any targeting error becomes exaggerated.

One alternative co-delivery option is for the carrier to achieve orbit insertion via aerocapture, and to design the carrier and probes to target identical atmospheric entry conditions. Aerocapture is the technique of flying through a planet's atmosphere to reduce the spacecraft's energy and capture into orbit, reducing the ΔV requirement compared to propulsive orbit insertion [18]. For this co-delivery method, the carrier and probes diverge in the atmosphere due to differences in their aerodynamic properties and control. By avoiding the need to set up two separate approach trajectories, this co-delivery technique reduces maneuver complexity during approach and eliminates a source of

*This assumption on total payload mass for a seismometer of the required sensitivity is based on the short-period instrument aboard the InSight lander and private communications with Mark Panning, Dec. 2021.

navigation error, while still gaining the benefits of delivering the probes from a single carrier spacecraft on an entry trajectory. Co-delivery of this kind is feasible at Mars for a range of entry conditions and vehicle types [19]. Modeling the error introduced to the trajectory of the carrier spacecraft due to these mechanical probe separations, and the impact of that error on a guided aerocapture trajectory, is a topic for future study.

Define the central entry state as the intersection of the approach trajectory with the atmospheric interface altitude of 125 km. As a reference point design for this study, assume entry latitude $\phi_0 = 7.5°$ North and longitude $\theta_0 = 151°$ East. The planet-relative entry velocity V_0 has magnitude $6.0\,\mathrm{km\,s^{-1}}$, entry flight-path angle $\gamma_0 = -12°$, and entry heading angle $\psi_0 = 80°$. Flight-path angle is the angle between the velocity vector and local horizontal, and heading angle (or azimuth) is the angle between the horizontal projection of the velocity vector and a due-North vector in that same plane (e.g. $\psi = 90°$ is due-East).

Assume the carrier spacecraft has properties similar to those of the Mars Science Laboratory (MSL) aeroshell: a 70° sphere-cone with offset center of gravity, giving $\beta = 130\,\mathrm{kg\,m^{-2}}$ and $L/D = 0.25$. In this scenario, the carrier could use lift modulation to aerocapture into an orbit with apoapsis altitude of up to about 1000 km from the same approach trajectory as the pre-separation probes [19]. Further analysis of this scenario, however, is beyond the scope of this study, which is focused on the probes themselves.

The trajectories in this study are numerically propagated using explicit Runge-Kutta integration of order 4(5) for a rotating ellipsoidal planet. Mars has gravitational parameter $\mu = 4.305 \times 10^4\ \mathrm{km^3\,s^{-2}}$, equatorial radius $R = 3397.2\,\mathrm{km}$, oblateness spherical harmonic coefficient $J_2 = 0.001964$, and a planetary rotation period of $\omega_p = 1.02595675$ days [20]. The equations of motion for the planet-relative state are provided in the appendix.

III. Varying Separation Magnitude and Timing

To gain initial insight into the design of these separation events, four probes are simulated with varying jettison speeds and separation times. The probes are back-propagated from the nominal entry state until the separation time, the probe velocity is updated corresponding to jettison speed and direction, and then the probes are propagated until impact with the Martian surface. The direction in which the jettison velocity is applied is also a key design choice; in this section, separation is considered along two orthogonal vectors, along-track and cross-track. The radial, cross-track, and along-track directions ($\hat{\boldsymbol{r}}$, $\hat{\boldsymbol{h}}$, and $\hat{\boldsymbol{\theta}}$, respectively) are defined in Eqs. 1–3 as functions of the position and *inertial* velocity vectors $\boldsymbol{r}$ and $\dot{\boldsymbol{r}}$, where $\dot{\boldsymbol{r}} = \boldsymbol{V} + \boldsymbol{\omega}_p \times \boldsymbol{r}$ and $\boldsymbol{\omega}_p = [0, 0, \omega_p]^T$. A pair of probes separates in the positive and negative directions along the along-track vector, and the same for the cross-track vector. The jettison speed varies from 5 to $40\,\mathrm{cm\,s^{-1}}$ at a nominal separation time of E-1 day, and the separation time varies from 0.25–3 days at a nominal V_j of $10\,\mathrm{cm\,s^{-1}}$. The resulting landing locations are shown to-scale in Figs. 1 and 2[†], and for each permutation the minimum and maximum great-circle distances between any two landing locations are shown in Table 1.

$$\hat{\boldsymbol{r}} = \frac{\boldsymbol{r}}{|\boldsymbol{r}|} \tag{1}$$

$$\hat{\boldsymbol{h}} = \frac{\boldsymbol{r} \times \dot{\boldsymbol{r}}}{|\boldsymbol{r} \times \dot{\boldsymbol{r}}|} \tag{2}$$

$$\hat{\boldsymbol{\theta}} = \hat{\boldsymbol{h}} \times \hat{\boldsymbol{r}} \tag{3}$$

Several useful relationships are reflected in these results. First, the along-track jettisons resulted in far greater separation distances than the cross-track jettisons.[‡] As a result of the 80° entry azimuth, the along-track jettisons correspond primarily to longitudinal separation, and cross-track jettisons primarily to latitudinal separation. Figures 1 and 2 emphasize this difference in scale. As shown in Table 1, distances between landing sites ranging from roughly 2.5 to 880 km are achieved from these separation events. Thus, jettison speeds on the order of $10\,\mathrm{cm\,s^{-1}}$ should be sufficient to deploy a network from this approach trajectory within the assumed constraints.

Furthermore, inspection of these results reveals a clear linear relationship between jettison speed and the resulting changes in landing location, and a similar linear relationship exists for separation time. This is an expected result despite the significant nonlinearity of the problem dynamics. The separation velocities are small enough that they can be treated as perturbations to the nominal trajectory, and these results imply that these perturbations are within the region about this reference where a linear approximation is valid. This linear relationship has significant implications for targeting

[†]The surface image is a mosaic created from data acquired by Viking Orbiter Imaging Systems and generated using MarsTrek, trek.nasa.gov/mars

[‡]Note that for these hyperbolic orbit states the radial and velocity directions are nearly aligned, so the along-track direction is significantly offset from the velocity direction; conceptualizing a direction in both the orbital plane and local horizontal plane, with the same sign as its projection onto the velocity vector, may be more intuitive.

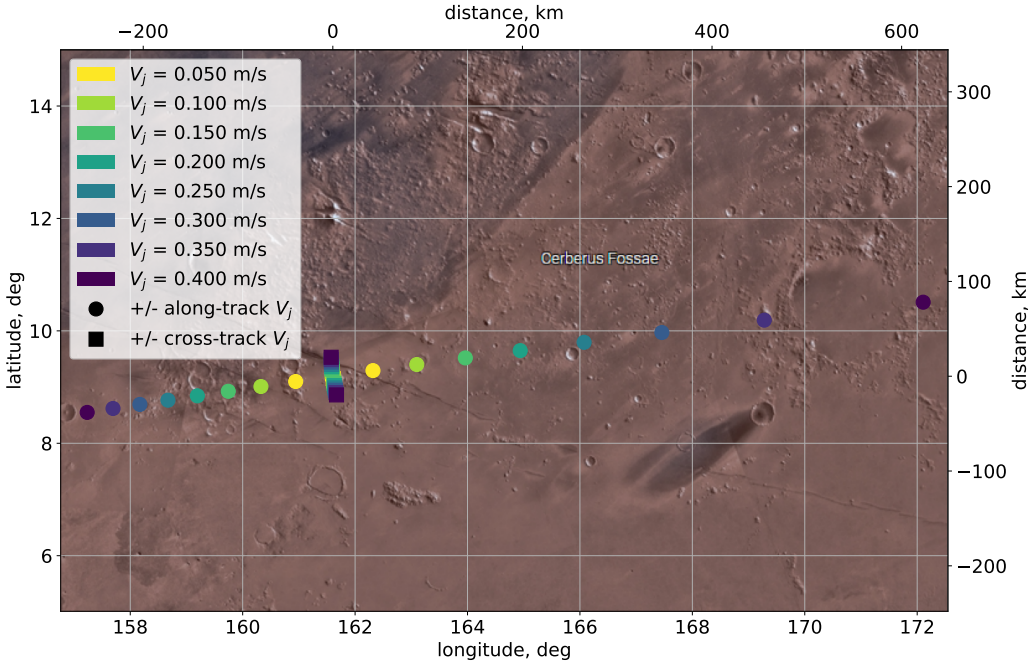

Fig. 1 Landing locations for varying V_j, separation at E-1 days, shown against to-scale Martian surface.

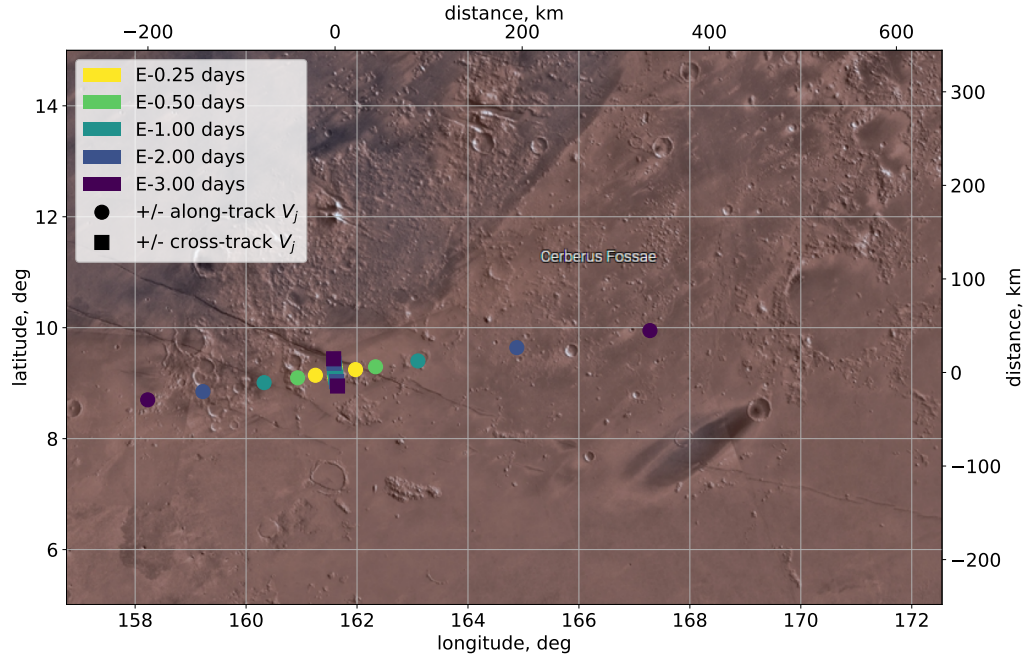

Fig. 2 Landing locations for varying separation time, $V_j = 10\,\mathrm{cm\,s^{-1}}$, shown against to-scale Martian surface.

Table 1 Landing site distances for four probes separated in ± along-track and cross-track directions for varying V_j and separation time

V_j, cm/s	Separation Time, days	Minimum Distance, km	Maximum Distance, km
5	E-1	5.014	81.315
10	E-0.25	2.697	42.767
10	E-0.5	5.159	83.072
10	E-1	10.028	163.926
10	E-2	19.710	334.440
10	E-3	29.366	534.907
15	E-1	15.042	249.332
20	E-1	20.056	339.516
25	E-1	25.070	437.490
30	E-1	30.083	548.555
35	E-1	35.096	684.054
40	E-1	40.108	877.297

network deployment; for example, within this linear regime, the scale of any network can be doubled by simply doubling the jettison speed *or* by doubling the time between separation and entry.

IV. Linearized Targeting Method

The linear relationships demonstrated by example in the previous section also enable application of a basic linearized targeting method to this problem. Take $\boldsymbol{x}_{\theta\phi} = [\theta, \phi]^T$ to be landing site coordinates and $\boldsymbol{V} = \boldsymbol{V}(t)$ to be the velocity of the probe at some time prior to landing. Apply a Taylor series expansion to $\boldsymbol{x}_{\theta\phi}$ about the trajectory of the carrier spacecraft, $\boldsymbol{x}^*_{\theta\phi}$, as a function of velocity, then neglect terms of second order or higher:

$$\boldsymbol{x}_{\theta\phi} = \boldsymbol{x}^*_{\theta\phi} + \left.\frac{\partial \boldsymbol{x}_{\theta\phi}}{\partial \boldsymbol{V}}\right|_* (\boldsymbol{V} - \boldsymbol{V}^*) + \text{H.O.T.s} \tag{4}$$

$$\Delta\boldsymbol{x}_{\theta\phi} \approx \left.\frac{\partial \boldsymbol{x}_{\theta\phi}}{\partial \boldsymbol{V}}\right|_* \boldsymbol{V}_j = [\boldsymbol{J}]\boldsymbol{V}_j \tag{5}$$

$$[\boldsymbol{J}] = \begin{bmatrix} \frac{\partial\theta}{\partial V_x} & \frac{\partial\theta}{\partial V_y} & \frac{\partial\theta}{\partial V_z} \\ \frac{\partial\phi}{\partial V_x} & \frac{\partial\phi}{\partial V_y} & \frac{\partial\phi}{\partial V_z} \end{bmatrix}_* \tag{6}$$

where the jettison velocity is the velocity of the probe minus the velocity of the carrier spacecraft at the moment after jettison, $\boldsymbol{V}_j = \boldsymbol{V} - \boldsymbol{V}^*$. The Jacobian matrix $[\boldsymbol{J}]$ can then be evaluated for any value of jettison time to represent the sensitivity of landing site coordinates to velocity at that time. By inverting the Jacobian, the $\boldsymbol{V}_j$ vector required to achieve a desired change in landing location, $\Delta\boldsymbol{x}_{\theta\phi}$, can be linearly approximated. The Jacobian in this case is not square, so the least-norm solution is selected to minimize V_j magnitude.

$$\boldsymbol{V}_j = [\boldsymbol{J}]^T ([\boldsymbol{J}][\boldsymbol{J}]^T)^{-1} \Delta\boldsymbol{x}_{\theta\phi} \tag{7}$$

For the purpose of this study, $[\boldsymbol{J}]$ is numerically approximated using first-order forward finite differencing; Eq. 8 gives an example for the first element of the matrix,

$$\frac{\partial\theta}{\partial V_x} = \frac{\theta_p - \theta^*}{\Delta V_x}, \tag{8}$$

where ΔV_x is a small velocity perturbation in the x-axis direction and θ_p is the landing site longitude that results from applying a jettison velocity of $[\Delta V_x, 0, 0]^T$ then propagating to surface impact. In this study, a perturbation value of $\Delta V_x = \Delta V_y = \Delta V_z = 1 \times 10^{-4}\,\mathrm{m\,s^{-1}}$ was selected.

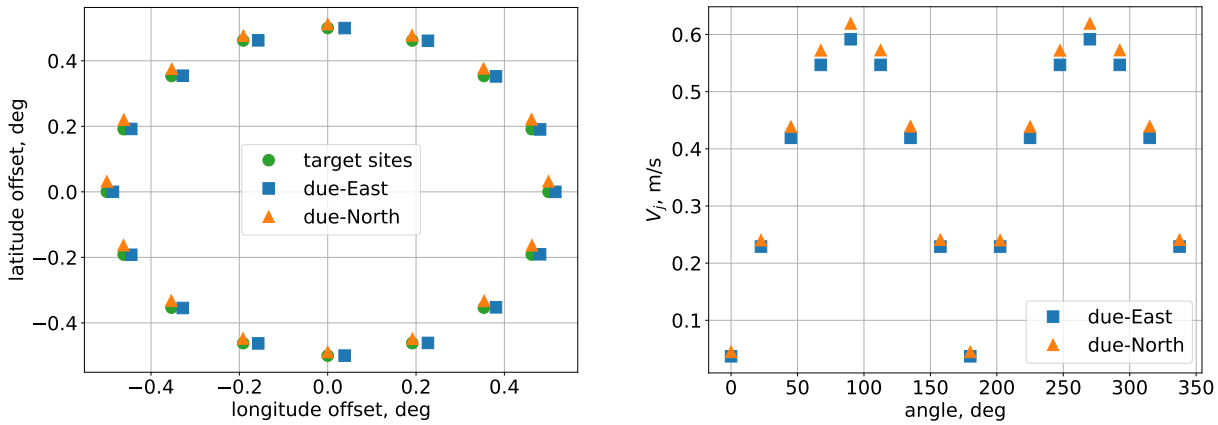

(a) Landing sites **(b) V_j as a function of angle**

Fig. 3 Linearized targeting demonstration, including both due-East and due-North carrier trajectories, for E-1 day separation time.

Numerically computing the Jacobian $[\boldsymbol{J}]$ according to Eqs. 6 and 8 allows one to linearly approximate the jettison velocity vector $\boldsymbol{V}_j$ required to achieve a shift in longitude and latitude equal to $\Delta\boldsymbol{x}_{\theta\phi} = [\Delta\theta, \Delta\phi]^T$ for a given separation time. To consider a different jettison time, the Jacobian is simply re-evaluated applying perturbations at that time.

This functionality is demonstrated in Fig. 3, where all targeting is for a jettison time of 1 day prior to entry. Two cases are shown, one with a due-East entry heading angle and the other with a due-North entry heading angle. Sixteen target landing locations are defined along a circle with radius 0.5°. The Jacobian is computed once for each case and then, for each target landing location, the jettison velocity is computed per Eq. 7 and applied to the state of the probe at the separation time, then the probe is propagated to the surface to compute the actual landing site. The achieved landing sites are compared with their targets in terms of degrees of offset from the central (unperturbed) landing site in Fig. 3a. Figure 3b shows the required jettison speed vs. the angle between the offset direction and the downrange velocity direction; that is, 0° is an offset in the downrange direction, 90° an offset in the crossrange direction, 180° in negative downrange, and 270° in negative crossrange.

The results in Fig. 3 demonstrate that linearized targeting works reasonably well for offsets within 0.5° of the central landing site. The jettison speeds required to shift the landing site along the crossrange direction are significantly greater than those required to shift along the downrange direction, as predicted by the results shown in Figs. 1 and 2. Crossrange offsets also incur greater targeting error for the same offset distance compared to downrange offsets, as is clear from the results in Fig. 3a; the due-East case has worse error for latitudinal offset, and the due-North case has worse error for longitudinal offset. Furthermore, this error is positive along the downrange direction for all landing targets considered here. The maximum error among all 32 targeting examples is 2.3 km. Finally, the $\boldsymbol{V}_j$ computed for downrange offset is mostly in the along-track direction and the $\boldsymbol{V}_j$ for crossrange offset is mostly in the cross-track direction, validating the assumption made for the results in Figs. 1 and 2 for this E-1 day separation event example.

Having demonstrated the effectiveness of this method, it is important to explore the bounds of the region in which linearization is a reasonable approximation for targeting. Figure 4 provides this result by computing the targeting error in terms of both coordinate angle and distance along the surface. The carrier trajectory in this case again uses the nominal 80° entry heading angle, and downrange and crossrange offset targets are again considered. The required jettison velocity for each targeting case is also computed and their magnitudes plotted; these magnitudes increase exactly linearly and the jettison directions are constant as a result of the linear targeting method.

Based on the results shown in Fig. 4, the upper limit of offset angles for which linearized targeting performs reasonably well is somewhere between 1° and 3°, depending on the application and level of acceptable error. Within 1° desired offset, error for the downrange targeting remains below 5 km and below 10 km for crossrange targeting; within 3° desired offset, the downrange and crossrange errors remain below 50 km and 100 km, respectively. After 4° or 5° of desired offset, both errors are increasingly rapidly, and by 6.5° to 7° of desired offset the probes begin missing the planet entirely when propagated using the jettison velocity computed by linearized targeting. Note that these results are all for a separation time of E-1 day.

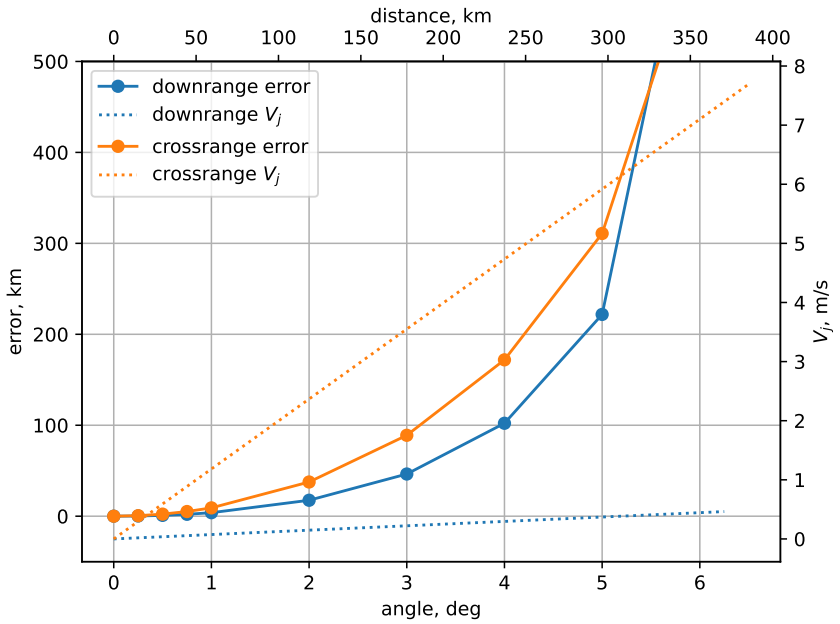

Fig. 4 Error and required V_j for linearized targeting for varying downrange and crossrange spacing. After the desired change in angle exceeds $6.5°$, both cases begin to miss the planet entirely.

V. Example Network Design

In this section an example network is designed that meets the stated assumptions and requirements, then a series of jettison events are computed using the results summarized in the preceding sections. This network includes three pairs of probes for a total of six landers in a symmetrical configuration on the surface. The timing of each jettison event is tuned in order to apply the same jettison speed for each pair of probes.

Because downrange separation is so much easier to achieve than crossrange, the two furthest probes are placed directly along the downrange track, offset from the center point by 1°; these points are labeled "A" and "-A." To avoid deploying the probes in a single line, the other two pairs must be away from the downrange track, yet still keep the crossrange offset small. To this end, a parallelogram shape is formed such that "B" and "-B" are each offset in a direction 45° from the downrange vector, and sites "C" and "-C" are each offset in a direction 30° from the downrange vector. The full nominal network is shown against a to-scale image of the Martian surface in Fig. 5 along with the central point (which is not actually targeted) and an arrow indicating the downrange direction projected onto the surface[§]. The network is located within the Cerberus Fossae region, and two semi-parallel fissures are visible in the surface image.

In order to target this network using a single jettison speed for all three separations, targeting is performed along a range of separation times to provide trends of required V_j; these results are shown in Fig. 6. As would be expected, required jettison speed increases dramatically as time between separation and entry approaches zero. A jettison speed of $10\,\mathrm{cm\,s^{-1}}$ is selected as a relatively low value that intersects all three curves between 0.5 and 5 days before entry; note that iterating between these results and the design of the network allows for flexibility in selection of the nominal jettison speed. A root solver is implemented to compute the precise jettison time for each probe that targets the desired landing location and results in a jettison speed equal to the desired value, with the approximate intersections of the curves with the dashed line in Fig. 6 providing good initial guesses for the solver. Finally, each probe trajectory is simulated, applying the nominal jettison event, and the distance between the desired and actual landing site is reported as the nominal error for each probe.

Table 2 summarizes the nominal results for this example network. The downrange and crossrange values are distances along the surface from the central point to the nominal landing location; the values for other probe in each pair are the same magnitudes and opposite signs. The computed jettison velocity direction is shown by components in the radial, along-track, and cross-track directions as dot products with the corresponding unit vectors, and the jettison time

[§]The surface image is a mosaic created from data acquired from the Context Camera aboard NASA's Mars Reconnaissance Orbiter and generated using MarsTrek, trek.nasa.gov/mars

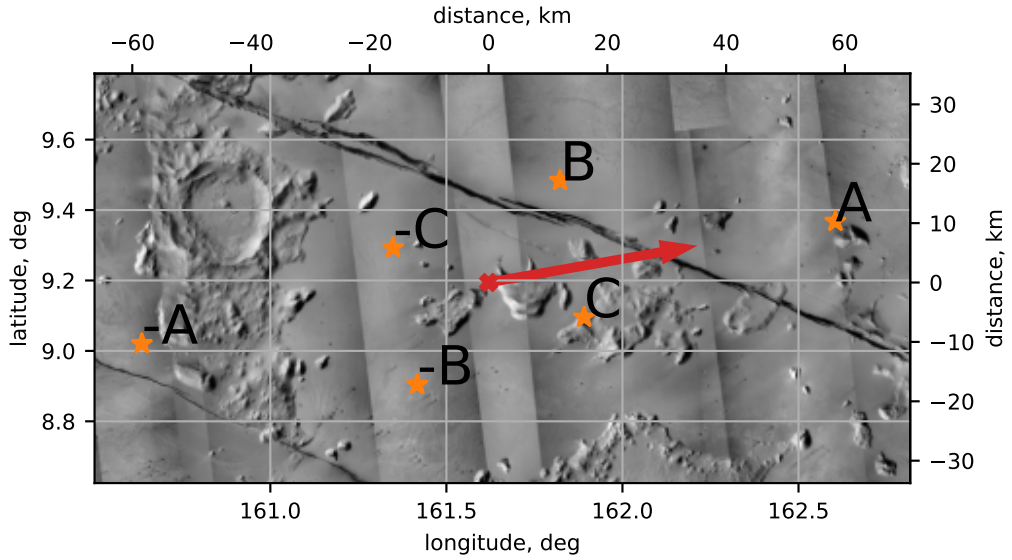

Fig. 5 Nominal landing locations for the example network shown with orange stars, with the downrange direction shown by a red arrow and the central point shown by a red X.

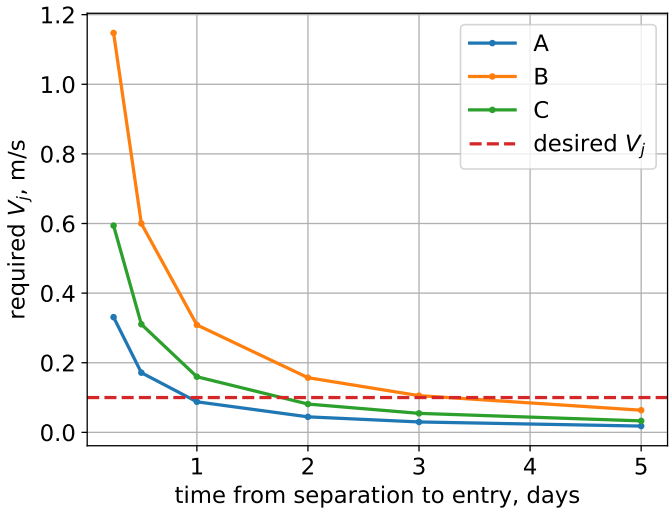

Fig. 6 Required V_j vs. separation time for the three chosen nominal landing sites.

Table 2 Properties of nominal network, jettison velocity and timing, and nominal targeting error

pair	downrange, km	crossrange, km	$\hat{\boldsymbol{V}}_j \cdot \hat{\boldsymbol{r}}$, m s^{-1}	$\hat{\boldsymbol{V}}_j \cdot \hat{\boldsymbol{\theta}}$, m s^{-1}	$\hat{\boldsymbol{V}}_j \cdot \hat{\boldsymbol{h}}$, m s^{-1}	t_j, days	nominal errors, km
A	59.292	0	0.00826	0.893	0.450	0.821	3.095, 3.804
B	14.823	14.823	0.0152	0.392	0.920	3.136	0.804, 0.841
C	14.823	-8.558	-0.0153	0.108	-0.994	1.651	0.370, 0.399

t_j for each pair of probes is given in days. Again, note that the other probes in each pair have the same jettison times and jettison velocities in the opposite directions. Finally, the nominal targeting errors are given for both probes in each pair, e.g. the errors for probes A and -A are 3.095 km and 3.804 km, respectively.

Probes A and -A have significantly more separation from the central point than the other two pairs. This is partly in order to spread out the computed jettison times without placing any jettison overly close to the time of entry; for a smaller downrange separation and the same jettison speed, the jettison time would occur even later (i.e. with an even smaller t_j). The jettison velocity for pair A is oriented mostly in the along-track direction, whereas pairs B and C jettison primarily in the cross-track directions; none of the three jettison velocities have large radial components. Even though pairs B and C both have at least as much downrange offset as crossrange, the jettison speed required to achieve crossrange is much higher, so it dominates the direction of jettison. Lastly, in this case the downrange pair, A, has significantly greater targeting error than the other probes. Although in general crossrange placements accumulate targeting error more quickly, the significantly greater total distance from the central point to pair A results in more linearization error. Since precision landing is not a requirement for these passive entry probes, nominal landing error within 5 km is likely acceptable.

VI. Monte Carlo Analysis

Having designed an example network and the jettison events required to deploy it, the impact of relevant uncertainties on the landing locations of all six probes is quantified next. Variability of atmospheric density is modeled by using random profiles of density vs. altitude that are generated using the 2010 version of the Mars Global Reference Atmospheric Model (Mars-GRAM 2010) [21]. Uncertainty in the approach trajectory of the carrier spacecraft is modeled by dispersing the state at atmospheric entry for each trial, then back-propagating the dispersed state to the time of first jettison. The entry flight-path angle γ_0 and entry velocity magnitude V_0 are dispersed independently according to Gaussian distributions centered at the nominal value and with some standard deviation σ. For this study, the 3σ value for γ_0 is set equal to the requirement on delivery error for MSL, and the 3σ value for V_0 is set equal to the required knowledge accuracy at EDL guidance system initialization for MSL [22]. For a given trial, these three dispersions are applied once, such that all six probes experience the same atmosphere and carrier spacecraft trajectory.

The ballistic coefficient of each probe is dispersed along a uniform distribution with bounds at ±5% of the nominal value; the lift-to-drag ratio always remains at its nominal value of zero, assuming that axisymmetric spin removes the effect of any small, unintended lift force. Finally, the magnitude of the jettison event is dispersed along a uniform distribution with bounds at ±10% of the nominal value; the direction of the jettison velocities are assumed to be nominal for the purpose of this study. These two dispersions are applied independently and randomly to each probe for each trial. Note that the dispersion on jettison velocities means pairs of probes will not be perfectly balanced during separation, and this would impart some undesired momentum to the carrier spacecraft and perturb its trajectory, with the velocity change of the carrier depending on its mass relative to the probes. These perturbations would result in additional error for any subsequent probe separations. Incorporating the effects of off-nominal jettison speeds on the carrier spacecraft is a topic for future study. These input dispersions are summarized in Table 3.

The goal is to deploy a network in approximately the correct geometry and location, rather than to precisely target each probe. Thus, the separate statistics of landing error for each probe do not directly relate to the performance requirements. To better characterize network delivery performance, define two error parameters, center error ε_c and shape error ε_s. Center error describes off-nominal location of the center of the network, and shape error describes

Table 3 Monte Carlo analysis input dispersions

Parameter	Dispersion
atmospheric density ρ	MarsGRAM
entry velocity magnitude V_0	3σ = 2m/s
entry flight-path angle γ_0	$3\sigma = 0.2^\circ$
probe ballistic coefficient β	±5%
jettison speed V_j	±10%

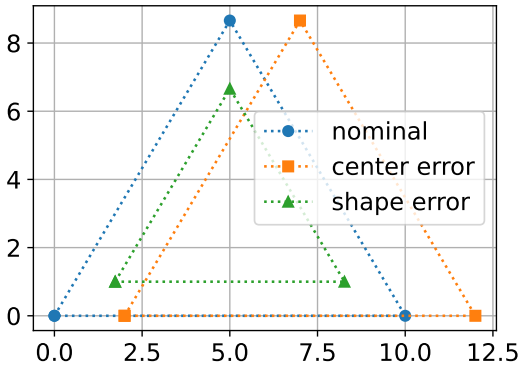

Fig. 7 Three example networks, illustrating center error vs. shape error

off-nominal distribution of probes around that center. Define center error for any given trial as follows:

$$\varepsilon_c = \sqrt{(\bar{\theta}^* - \bar{\theta})^2 + (\bar{\phi}^* - \bar{\phi})^2} \tag{9}$$

where $\bar{\theta}^*$ and $\bar{\phi}^*$ are the average longitude and latitude, respectively, across all probe locations for the *nominal* network design, and $\bar{\theta}$ and $\bar{\phi}$ are the average longitude and latitude of the actual probe landing sites. This error is computed in radians and can be converted to distance by multiplying by the planet's radius. To compute the shape error, compute the great circle distance between every unique pair of landing sites, yielding $d = N(N-1)/2$ distances for N probes, and label these values δ_i^* and δ_i for the nominal and actual landing sites, respectively. The shape error is then defined as the root sum squared of the differences between the nominal distance and actual distance for each unique pair of landing sites, divided by the total number of probes N:

$$\varepsilon_s = \frac{\sqrt{(\delta_1^* - \delta_1)^2 + \ldots + (\delta_d^* - \delta_d)^2}}{N}, \qquad d = \frac{N(N-1)}{2} \tag{10}$$

A more intuitive representation of these parameters is provided by Fig. 7, which shows a basic nominal network in blue circles. The orange squares have the correct network shape but all points are shifted to the right, resulting in $\varepsilon_c = 2$ and $\varepsilon_s = 0$. The green triangles are centered correctly but the entire geometry has been reduced in size, resulting in $\varepsilon_c = 0$ and $\varepsilon_s = 2$.

The results of the 5000-trial Monte Carlo analysis are summarized in Fig. 8 and Table 4. The landing site for each probe and the central point of those sites are shown in Fig. 8 for every trial. The nominal landing sites and central point are shown in the figure, along with the landing site locations for the trial that resulted in the worst shape error, about 6 km. Statistics of the center and shape errors are given in Table 4. Additionally, for every trial the great circle distance is computed between every unique pair of landing sites and then the minimum, maximum, and average of these distances is recorded; the statistics of these values are also shown in the table.

The large spread of landing locations shown in Fig. 8, especially in both directions along the downrange vector, is an expected result for passive entry vehicles subject to a number of dispersions. Considering that the nominal network includes probes separated by less than 20 km, the landing site dispersions of $\pm 10 - 25$ km downrange would seem to preclude successful deployment of this network. However, as captured by statistics of the center and shape error parameters, these dispersions are mostly applied to the network as a whole, shifting the entire network with only minor distortions to its shape. Indeed, the worst-case scenario for shape error shown in Fig. 8 is still clearly recognizable as the desired network shape. As reported in Table 4, the closest that two probes ever land in any single trial is 20 km, and the farthest in any trial is about 137 km; this performance is well within the assumed requirement of placing probes between 10 and 200 km apart on the surface.

These favorable results occur because most of the landing site variation is due to dispersions in entry flight-path angle and atmospheric density, and these affect all of the probes more or less equally. While a $\pm 10\%$ variation in jettison speed is significant and is applied independently to each probe, the actual jettison speeds are relatively small at a nominal value of 10 cm s^{-1}. A ± 1 cm s^{-1} change in velocity applied within 5 days of entry is small enough that it has

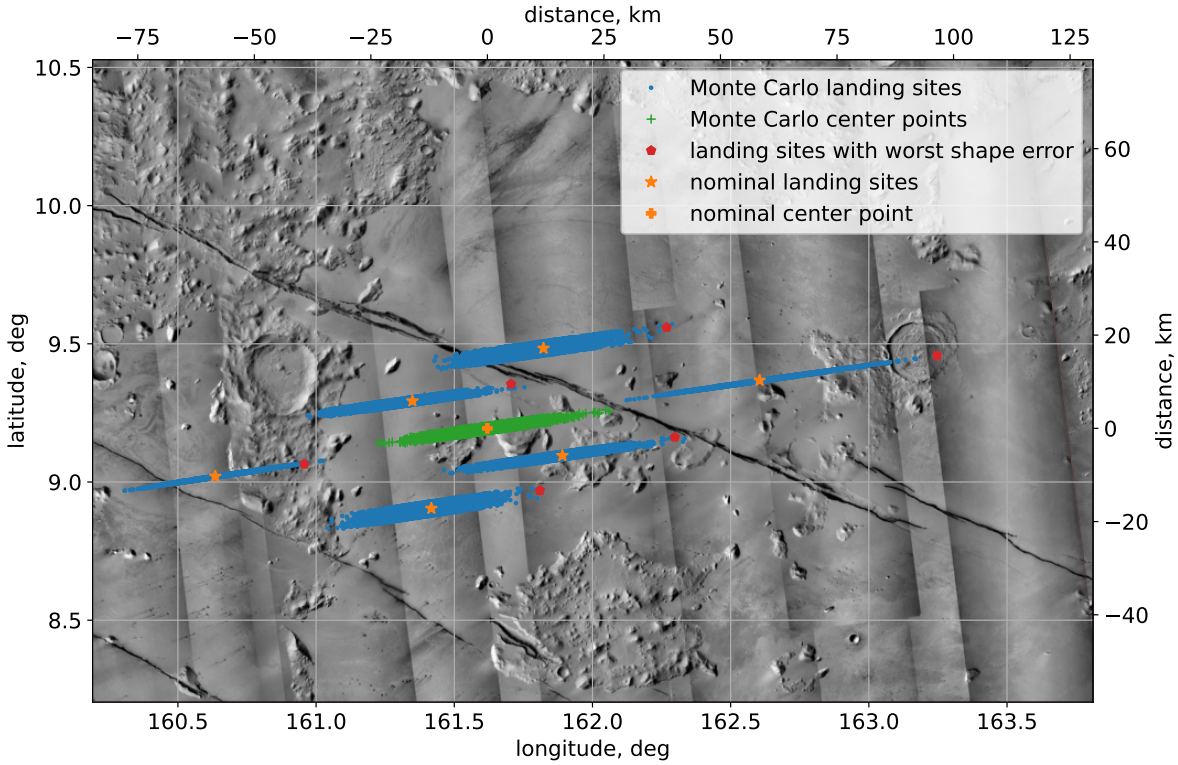

Fig. 8 Nominal and random trial landing locations shown against to-scale Martian surface.

Table 4 Statistics of relative landing site separation distances

Parameter	Mean	Min.	Max.	3σ
center error ε_c, km	5.309	0.012	26.344	12.102
shape error ε_s, km	2.285	0.366	6.055	2.859
min. separation, km	21.741	20.000	24.113	2.363
max. separation, km	118.808	103.312	137.478	17.011
avg. separation, km	52.168	46.583	59.441	5.924

a relatively minor impact on the resulting network geometry for this scenario. Furthermore, by keeping the probes relatively close together but putting the probes that are offset in only downrange the furthest away, the design of this nominal network makes it more robust to changes in probe locations without violating the requirements on network placement. The center of the network does vary significantly, but a starting assumption is that this is allowable, as may well be the case for something like a regional seismic network in Cerberus Fossae, a fairly large region.

VII. Conclusion

The results in this paper provide insight into the design of a regional network of rough landers for Mars. The demonstration of linearity enables a mission designer to use simple intuition such as doubling the jettison velocities to double the size of the network, and the bounds of the region where this linear relationship is valid were quantified. The linearized targeting method is readily applied to any number of probes and desired network geometry, and could be incorporated with root-solvers or other optimization tools to rapidly explore the trade space. The Monte Carlo analysis demonstrates that large dispersions in probe landing locations do not necessarily translate into large errors on the shape or scale of the resulting network, an insight aided by the definition of separate center and shape error parameters.

Appendix

Take the position coordinates to be radial distance r, longitude θ, and geocentric latitude ϕ. Take the planet-relative velocity coordinates to be velocity magnitude V, flight-path angle γ, and heading angle ψ. The equations of motion for a vehicle in atmospheric flight around an ellipsoidal rotating planet are given below:

$$\dot{r} = V \sin\gamma \tag{11a}$$

$$\dot{\theta} = \frac{V \cos\gamma \sin\psi}{r \cos\phi} \tag{11b}$$

$$\dot{\phi} = \frac{V \cos\gamma \cos\psi}{r} \tag{11c}$$

$$\begin{aligned}\dot{V} = &-D - g_r \sin\gamma - g_\phi \cos\gamma \cos\psi \\ &+ \omega_p^2 r \cos\phi \left(\cos\phi \sin\gamma - \sin\phi \cos\gamma \cos\psi\right)\end{aligned} \tag{12a}$$

$$\begin{aligned}\dot{\gamma} = \frac{1}{V}\Bigg[&L\cos\sigma + \cos\gamma\left(\frac{V^2}{r} - g_r\right) + g_\phi \sin\gamma\cos\psi + 2\omega_p V \cos\phi \sin\psi \\ &+ \omega_p^2 r \cos\phi \left(\cos\phi\cos\gamma + \sin\phi\sin\gamma\cos\psi\right)\Bigg]\end{aligned} \tag{12b}$$

$$\begin{aligned}\dot{\psi} = \frac{1}{V}\Bigg[&\frac{L\sin\sigma}{\cos\gamma} + \frac{V^2}{r}\tan\phi\cos\gamma\sin\psi + g_\phi \frac{\sin\psi}{\cos\gamma} \\ &- 2\omega_p V\left(\cos\phi\tan\gamma\cos\psi - \sin\phi\right) + \frac{\omega_p^2 r}{\cos\gamma}\cos\phi\sin\phi\sin\psi\Bigg]\end{aligned} \tag{12c}$$

where

$$L = \frac{\rho V^2}{2\beta} L/D \tag{13a}$$

$$D = \frac{\rho V^2}{2\beta} \tag{13b}$$

$$g_r = \frac{\mu}{r^2}\left[1 + \frac{3J_2 R^2}{2r^2}\left(1 - 3\sin^2\phi\right)\right] \tag{13c}$$

$$g_\phi = \frac{\mu}{r^2}\left[\frac{3J_2 R^2}{2r^2} 2\sin\phi\cos\phi\right] \tag{13d}$$

Acknowledgments

This work was supported by a NASA Space Technology Research Fellowship. S. W. Albert acknowledges ideas and advice from other participants in the Revolutionizing Access to the Martian Surface workshop organized by the W. M. Keck Institute for Space Studies, as well as input from Mark Panning, Dan Burkhart, and Robert Braun.

References

[1] Culbert, C., Ehlmann, B., and Fraeman, A., "Revolutionizing Access to the Martian Surface," Tech. rep., Keck Institute for Space Studies, Caltech, 2021. In press.

[2] Nunn, C., Pike, W. T., Standley, I. M., Calcutt, S. B., Kedar, S., and Panning, M. P., "Standing on Apollo's Shoulders: a Microseismometer for the Moon," *The Planetary Science Journal*, Vol. 2, No. 1, 2021, p. 36.

[3] Rafkin, S., "The Atmospheric Characterization for Exploration and Science (ACES) instrument suite for Mars," *2015 IEEE Aerospace Conference*, 2015, pp. 1–6. https://doi.org/10.1109/AERO.2015.7119061.

[4] Scoon, G. E. N., and Whitcomb, G. P., "MARSNET: A precursor to the surface exploration of Mars," *Acta Astronautica*, Vol. 29, No. 10, 1993, pp. 823–831. https://doi.org/10.1016/0094-5765(93)90164-R, world Space Congress.

[5] Squyres, S., "The Mars environmental survey (mesur) mission," *Advances in Space Research*, Vol. 15, No. 4, 1995, pp. 179–188. https://doi.org/10.1016/0273-1177(94)00079-G.

[6] Harri, A.-M., Linkin, V., Polkko, J., Marov, M., Pommereau, J.-P., Lipatov, A., Siili, T., Manuilov, K., Lebedev, V., Lehto, A., Pellinen, R., Pirjola, R., Carpentier, T., Malique, C., Makarov, V., Khloustova, L., Esposito, L., Maki, J., Lawrence, G., and Lystsev, V., "Meteorological Observations on Martian Surface: Met-Packages of Mars-96 Small Stations and Penetrators," *Planetary and Space Science*, Vol. 46, No. 6, 1998, pp. 779–793. https://doi.org/10.1016/S0032-0633(98)00012-9.

[7] Banderdt, B., Chicarro, A. F., Coradini, M., Federico, C., Greeley, R., Hechler, M., Knudsen, J. M., Leovy, C., Lognonne, P., Lowry, L., McCleese, D., McKay, C., Pellinen, R., Phillips, R., Scoon, G. E. N., Spohn, T., Squyres, S., Taylor, F., and Wanke, H., "INTERMARSNET: Phase-A Study Report," Tech. Rep. ESA Publication D/SCI(96)2, European Space Agency, April 1996.

[8] Smrekar, S., Catling, D., Lorenz, R., Magalhães, J., Moersch, J., Morgan, P., Murray, B., Presley, M., Yen, A., Zent, A., and Blaney, D., "Deep Space 2: The Mars Microprobe Mission," *Journal of Geophysical Research: Planets*, Vol. 104, No. E11, 1999, pp. 27013–27030. https://doi.org/10.1029/1999JE001073.

[9] Harri, A.-M., Marsal, O., Lognonne, P., Leppelmeier, G., Spohn, T., Glassmeier, K.-H., Angrilli, F., Banerdt, W., Barriot, J., Bertaux, J.-L., Berthelier, J., Calcutt, S., Cerisier, J., Crisp, D., Dehant, V., Giardini, D., Jaumann, R., Langevin, Y., Menvielle, M., Musmann, G., Pommereau, J., Di Pippo, S., Guerrier, D., Kumpulainen, K., Larsen, S., Mocquet, A., Polkko, J., Runavot, J., Schumacher, W., Siili, T., Simola, J., and Tillman, J., "Network science landers for Mars," *Advances in Space Research*, Vol. 23, No. 11, 1999, pp. 1915–1924. https://doi.org/10.1016/S0273-1177(99)00279-3.

[10] Harri, A. M., Schmidt, W., Linkin, V., Alexashkin, S., and Vazquez, L., "MetNet Mars Mission – New Lander Generation for Martian in situ Surface Observations," *European Planetary Science Congress*, 2012.

[11] Braun, R. D., and Manning, R. M., "Mars Exploration Entry, Descent, and Landing Challenges," *Journal of Spacecraft and Rockets*, Vol. 44, No. 2, 2007.

[12] Giardini, D., Lognonné, P., Banerdt, W. B., Pike, W. T., Christensen, U., Ceylan, S., Clinton, J. F., van Driel, M., Stähler, S. C., Böse, M., Garcia, R. F., Khan, A., Panning, M., Perrin, C., Banfield, D., Beucler, E., Charalambous, C., Euchner, F., Horleston, A., Jacob, A., Kawamura, T., Kedar, S., Mainsant, G., Scholz, J.-R., Smrekar, S. E., Spiga, A., Agard, C., Antonangeli, D., Barkaoui, S., Barrett, E., Combes, P., Conejero, V., Daubar, I., Drilleau, M., Ferrier, C., Gabsi, T., Gudkova, T., Hurst, K., Karakostas, F., King, S., Knapmeyer, M., Knapmeyer-Endrun, B., Llorca-Cejudo, R., Lucas, A., Luno, L., Margerin, L., McClean, J. B., Mimoun, D., Murdoch, N., Nimmo, F., Nonon, M., Pardo, C., Rivoldini, A., Manfredi, J. A. R., Samuel, H., Schimmel, M., Stott, A. E., Stutzmann, E., Teanby, N., Warren, T., Weber, R. C., Wieczorek, M., and Yana, C., "The seismicity of Mars," *Nature Geoscience*, Vol. 13, No. 3, 2020, pp. 205–212. https://doi.org/10.1038/s41561-020-0539-8.

[13] Kedar, S., Panning, M. P., Smrekar, S. E., Stähler, S. C., King, S. D., Golombek, M. P., Manga, M., Julian, B. R., Shiro, B., Perrin, C., Power, J. A., Michaut, C., Ceylan, S., Giardini, D., Lognonné, P. H., and Banerdt, W. B., "Analyzing Low Frequency Seismic Events at Cerberus Fossae as Long Period Volcanic Quakes," *Journal of Geophysical Research: Planets*, Vol. 126, No. 4, 2021, p. e2020JE006518. https://doi.org/https://doi.org/10.1029/2020JE006518.

[14] Lognonné, P., Banerdt, W. B., Giardini, D., Pike, W. T., Christensen, U., Laudet, P., de Raucourt, S., Zweifel, P., Calcutt, S., Bierwirth, M., Hurst, K. J., Ijpelaan, F., Umland, J. W., Llorca-Cejudo, R., Larson, S. A., Garcia, R. F., Kedar, S., Knapmeyer-Endrun, B., Mimoun, D., Mocquet, A., Panning, M. P., Weber, R. C., Sylvestre-Baron, A., Pont, G., Verdier, N., Kerjean, L., Facto, L. J., Gharakanian, V., Feldman, J. E., Hoffman, T. L., Klein, D. B., Klein, K., Onufer, N. P., Paredes-Garcia, J., Petkov, M. P., Willis, J. R., Smrekar, S. E., Drilleau, M., Gabsi, T., Nebut, T., Robert, O., Tillier, S., Moreau, C., Parise, M., Aveni, G., Ben Charef, S., Bennour, Y., Camus, T., Dandonneau, P. A., Desfoux, C., Lecomte, B., Pot, O., Revuz, P., Mance, D., tenPierick, J., Bowles, N. E., Charalambous, C., Delahunty, A. K., Hurley, J., Irshad, R., Liu, H., Mukherjee, A. G., Standley, I. M., Stott, A. E., Temple, J., Warren, T., Eberhardt, M., Kramer, A., Kühne, W., Miettinen, E.-P., Monecke, M., Aicardi, C., André, M., Baroukh, J., Borrien, A., Bouisset, A., Boutte, P., Brethomé, K., Brysbaert, C., Carlier, T., Deleuze, M., Desmarres, J. M., Dilhan, D., Doucet, C., Faye, D., Faye-Refalo, N., Gonzalez, R., Imbert, C., Larigauderie, C., Locatelli, E., Luno, L., Meyer, J.-R., Mialhe, F., Mouret, J. M., Nonon, M., Pahn, Y., Paillet, A., Pasquier, P., Perez, G., Perez, R., Perrin, L., Pouilloux, B., Rosak, A., Savin de Larclause, I., Sicre, J., Sodki, M., Toulemont, N., Vella, B., Yana, C., Alibay, F., Avalos, O. M., Balzer, M. A., Bhandari, P., Blanco, E., Bone, B. D., Bousman, J. C., Bruneau, P., Calef, F. J., Calvet, R. J., D'Agostino, S. A., de los Santos, G., Deen, R. G., Denise, R. W., Ervin, J., Ferraro, N. W., Gengl, H. E., Grinblat, F., Hernandez, D., Hetzel, M., Johnson, M. E., Khachikyan, L., Lin, J. Y., Madzunkov, S. M., Marshall, S. L., Mikellides, I. G., Miller, E. A., Raff, W., Singer, J. E., Sunday, C. M., Villalvazo, J. F., Wallace, M. C., Banfield, D., Rodriguez-Manfredi, J. A., Russell, C. T., Trebi-Ollennu, A., Maki, J. N., Beucler, E., Böse, M., Bonjour, C., Berenguer, J. L., Ceylan, S., Clinton, J., Conejero,

V., Daubar, I., Dehant, V., Delage, P., Euchner, F., Estève, I., Fayon, L., Ferraioli, L., Johnson, C. L., Gagnepain-Beyneix, J., Golombek, M., Khan, A., Kawamura, T., Kenda, B., Labrot, P., Murdoch, N., Pardo, C., Perrin, C., Pou, L., Sauron, A., Savoie, D., Stähler, S., Stutzmann, E., Teanby, N. A., Tromp, J., van Driel, M., Wieczorek, M., Widmer-Schnidrig, R., and Wookey, J., "SEIS: Insight's Seismic Experiment for Internal Structure of Mars," *Space Science Reviews*, Vol. 215, No. 1, 2019, p. 12. https://doi.org/10.1007/s11214-018-0574-6.

[15] Hopf, T., Kumar, S., Karl, W., and Pike, W., "Shock protection of penetrator-based instrumentation via a sublimation approach," *Advances in Space Research*, Vol. 45, No. 3, 2010, pp. 460–467. https://doi.org/10.1016/j.asr.2009.08.015.

[16] Barba, N., Komarek, T., Woolley, R., Giersch, L., Stamenković, V., Gallagher, M., and Edwards, C. D., "Mars Small Spacecraft Studies: Overview," *2019 IEEE Aerospace Conference*, 2019, pp. 1–10. https://doi.org/10.1109/AERO.2019.8741735.

[17] Braun, R. D., Mitcheltree, R. A., and Cheatwood, F. M., "Mars Microprobe Entry-to-Impact Analysis," *Journal of Spacecraft and Rockets*, Vol. 36, No. 3, 1999, pp. 412–420. https://doi.org/10.2514/2.3461.

[18] Hall, J. L., Noca, A. N., and Bailey, R. W., "Cost-Benefit Analysis of the Aerocapture Mission Set," *Journal of Spacecraft and Rockets*, Vol. 42, No. 2, 2005, pp. 309–320.

[19] Albert, S. W., Braun, R. D., and Schaub, H., "Flight Mechanics Feasibility Assessment for Co-Delivery of Direct-Entry Probe and Aerocapture Orbiter," *Submitted to Journal of Spacecraft and Rockets*, 2021.

[20] Vallado, D. A., *Fundamentals of Astrodynamics and Applications*, 4^{th} ed., Microcosm Press, 2013, Chap. Appendix D, pp. 1041–1042.

[21] Justh, H., "Mars Global Reference Atmospheric Model 2010 Version: Users Guide," Tech. Rep. NASA/TM—2014–217499, NASA, 2014.

[22] Martin-Mur, T. J., Kruizinga, G. L., Burkhart, P. D., Abilleira, F., Wong, M. C., and Kangas, J. A., "Mars Science Laboratory Interplanetary Navigation," *Journal of Spacecraft and Rockets*, Vol. 51, No. 4, 2014, pp. 1014–1028. https://doi.org/10.2514/1.A32631.